ChemPubSoc Europe

DOI: 10.1002/chem.201405039

CHEMISTRY A European Journal Full Paper

Solar Energy Conversion

Layer-by-Layer Assemblies of Catechol-Functionalized TiO_2 Nanoparticles and Porphyrins through Electrostatic Interactions

Alexandra Burger,[a] Rubén D. Costa,[b] Volodymyr Lobaz,[c] Wolfgang Peukert,[c] Dirk M. Guldi,[b] and Andreas Hirsch*[a]

Abstract: In the current work, we present the successful functionalization and stabilization of P-25 TiO_2 nanoparticles by means of N1,N7-bis(3-(4-*tert*-butyl-pyridium-methyl)phenyl)-4-(3-(3-(4-*tert*-butyl-pyridinium-methyl)phenylamino)-3-oxopropyl)-4-(3,4-dihydroxybenzamido)heptanediamide tribromide (**1**). The design of the latter is aimed at nanoparticle functionalization and stabilization with organic building blocks. On one hand, **1** features a catechol anchor to enable its covalent grafting onto the TiO_2 surface, and on the other hand, positively charged pyridine groups at its periphery to prevent TiO_2 agglomeration through electrostatic repulsion. The success of functionalization and stabilization was corroborated by thermogravimetric analysis, dynamic light-scattering, and zeta potential measurements. As a complement to this, the formation of layer-by-layer assemblies, which are governed by electrostatic interactions, by alternate deposition of functionalized TiO_2 nanoparticles and two negatively charged porphyrin derivatives, that is, 5,10,15,20-(phenoxyacetic acid)-porphyrin (**2**) and 5,10,15,20-(4-(2-ethoxycarbonyl)-4-(2-phenoxyacetamido)heptanedioic acid)-porphyrin (**3**), is documented. To this end, the layer-by-layer deposition is monitored by UV/Vis spectroscopy, scanning electron microscopy, ellipsometry, and profilometry techniques. The resulting assemblies are utilized for the construction and testing of novel solar cells. From stable and repeatable photocurrents generated during several "on-off" cycles of illumination, we derive monochromatic incident photo-to-current conversion efficiencies of around 3%.

Introduction

The supramolecular construction of hierarchically ordered, layered architectures is currently an emerging field. Most notably, it opens up facile access to new functional hybrid devices with potential applications in, for example, solar energy conversion,[1] drug delivery,[2] electrochromic films,[3] membranes,[4] or hydrogen generation.[5] In particular, the development of layered organic-hybrid components represents a tremendous challenge, because the characteristics of both classes of compounds may be combined synergetically, giving more than the simple sum of the individual components.

One possible method for building up layered architectures relies on the layer-by-layer (LbL) technique,[6] through which multilayer assemblies are realized by employing electrostatic attractions between oppositely charged building blocks. The LbL technique was first used by Decher et al. to build up multilayers of charged polymers by alternate dipping of substrates into solutions of either positively or negatively charged polymers. Repeatedly performed cycles of this procedure lead to multiple polymer layers, which are stabilized by electrostatic interactions.[7] In light of the latter, the LbL technique constitutes a very simple, but efficient method for the consecutive deposition of individual molecular layers onto planar solid supports to build up multilayer architectures.

In recent years, a myriad of functional architectures with unique mechanical, optical, electrical, and biological properties have been designed in this way.[4,6b,8] In general, either polyelectrolytes[9] or charged organic molecules[10] have been used as components for the construction of LbL multilayers. Combined LbL assemblies of organic electrolytes with charged inorganic nanoparticles (NPs) have also been constructed.[2b,11] For example, Pichon et al. developed magneto-tunable hybrid films of iron oxide nanoparticles and alternating PAH/PSS layers,[12] Kotov et al. reported polyelectrolyte/semiconductor nanoparticle composites,[13] and Schmitt et al. focused on polyelectrolyte/Au nanoparticle composites.[14] Examples of LbL assemblies of NPs and graphene oxide have also been reported,[15] but LbL assemblies of organic molecules and nanoparticles have so far been elusive. This is where our current work makes a significant contribution.

[a] *A. Burger, Prof. Dr. A. Hirsch*
Department of Chemistry and Pharmacy
Friedrich-Alexander Universität Erlangen-Nürnberg
Institute of Organic Chemistry
Henkestrasse 42, 91054 Erlangen (Germany)
E-mail: andreas.hirsch@fau.de

[b] *Dr. R. D. Costa, Prof. Dr. D. M. Guldi*
Department of Chemistry and Pharmacy
Friedrich-Alexander Universität Erlangen-Nürnberg
Interdisciplinary Center for Molecular Materials
Egerlandstrasse 3, 91058 Erlangen (Germany)

[c] *Dr. V. Lobaz, Prof. Dr. W. Peukert*
Friedrich-Alexander Universität Erlangen-Nürnberg
Institute of Particle Technology
Cauerstrasse 4, 91058 Erlangen (Germany)

One of the most prominent inorganic building blocks for the construction of hybrid materials are TiO_2 NPs, which exhibit a variety of favorable chemical and physical properties as well as chemical inertness, negligible solubility in water or protic solvents, and pronounced pH tolerance.[16] TiO_2 is a wide-bandgap semiconductor material, which has been used as a photocatalyst for the degradation of pollutants, for photocatalytic oxidation, and for water splitting. Most importantly, it represents the inorganic semiconductor component in dye-sensitized solar cells.[17] Porphyrins are widely used as organic sensitizers in the latter.[18] TiO_2/porphyrin composites range from porphyrins bound to TiO_2 through one single anchor group, to anionic porphyrins adsorbed on porous TiO_2 electrodes through multiple anchor groups.[19] Additionally, metalloporphyrins can be coordinated to TiO_2 through axial metal–ligand coordination to surface-bound isonicotinic acid and its derivatives.[20] Moreover, porphyrins have been assembled to TiO_2 by using the Langmuir–Blodgett technique,[21] as well as through the construction of metal-organic frameworks.[22] Our work describes the formation of TiO_2 NPs/porphyrin composites built up through electrostatic interactions, using the LbL technique.

With NPs featuring different, size-dependent properties compared with those of bulk materials, one setback is their strong tendency to form agglomerates, which has to be overcome to preserve their unique properties. To this end, steric and/or electrostatic repulsions through chemical surface functionalization constitute a powerful approach.[8b,23] Chemical surface functionalization of NPs with, for example, organic building blocks through chemisorption has a number of conceptual advantages over the physical immobilization of molecular building blocks onto the surface of NPs by means of electrostatic- and/or dipole–dipole interaction driven physisorption.[24] Notably, depending on the stabilizers, agglomeration processes, and the solubility of the NPs are controlled, and their electronic, magnetic, and optical properties are tuned as they are attached covalently to the surface.[25] In terms of organic stabilizers, polymers, oligomers, and also small molecules have been probed, which introduce either steric or electrostatic repulsions or a combination of both.[7,26]

For the covalent functionalization of metal oxide NPs, catechol groups have emerged recently as a very potent anchor, yielding highly stable and soluble coupling products.[27] Nevertheless, the preparation of catechol derivatives bearing charged groups to enable the functionalization and stabilization of NPs in solutions has barely been explored. A notable exception is our recent report on the synthesis of cationic dendrons equipped with catechol anchors.[28] Here, besides the demonstration of the successful functionalization of ZnO NPs, photoelectrochemical cells were fabricated, in which mesoporous ZnO films were functionalized with these cationic dendrons and subsequently sensitized with an anionic porphyrin.

In the current work, we demonstrate not only the formation of double-layer architectures, but also the construction of multiple-layer architectures governed by electrostatic interactions between catechol-functionalized P25-TiO_2 NPs and anionic porphyrins through the LbL technique.

We also report for the first time the functionalization of P25-TiO_2 NPs with a positively charged catechol-based building block, that is, N1,N7-bis(3-(4-*tert*-butyl-pyridium-methyl)phenyl)-4-(3-(3-(4-*tert*-butyl-pyridinium-methyl)phenylamino)-3-oxopropyl)-4-(3,4-dihydroxybenzamido)heptanediamide tribromide (**1**). This paves the way for the formation of stable NPs (Scheme 1a). The functionalization of NPs with a single functional building block such as **1** allows the control of the number of charges introduced onto the surface, as well as the thickness of the organic layer on the particle surface. The latter features are in contrast to those of previously reported NPs, which are functionalized with just polymers. The dendritic branching in **1** places steric hindrance as well as three positive charges, formed by quaternized pyridines, onto the periphery of the NPs.

As a complement to the functionalized, positively charged TiO_2 NPs, negatively charged porphyrins have been synthesized. With porphyrins featuring characteristic absorption bands, they can function as ideal reporters in the successive analysis of the LbL assembly. In this regard, we focused on the synthesis of two porphyrins, namely 5,10,15,20-(phenoxyacetic acid)-porphyrin (**6**) and 5,10,15,20-(4-(2-ethoxycarbonyl)-4-(2-phenoxyacetamido)heptanedioic acid)-porphyrin (**8**). Both are free-base tetraphenyl porphyrin derivatives, which differ in the number of carboxylic acids at the phenyl rings: 4 versus 12 in **6** and **8**, respectively. These oligo-carboxylic acid porphyrins are transformed easily into the corresponding oligo-carboxylates after deprotonation (see Scheme 1b, porphyrins **2** and **3**, respectively). The formation of multilayer architectures was demonstrated by using positively charged TiO_2 NPs and the negatively charged porphyrins **2** and **3**. (Scheme 1c).

Results and Discussion

Synthesis and characterization of 5,10,15,20-(phenoxyacetic acid)-porphyrin (6) and 5,10,15,20-(4-(2-ethoxycarbonyl)-4-(2-phenoxyacetamido)heptanedioic acid-)porphyrin (8)

For the development of oligo-carboxylated porphyrins, which can be transformed easily into oligo-anions after deprotonation, we focused on the synthesis of two systems, namely 5,10,15,20-(phenoxyacetic acid)-porphyrin (**6**) and 5,10,15,20-(4-(2-ethoxycarbonyl)-4-(2-phenoxyacetamido)heptanedioic acid)-porphyrin (**8**) (Scheme 2). Both are free-base tetraphenylporphyrin derivatives, which differ in the number of carboxylic groups connected to the phenyl rings. Compound **6** contains four, whereas **8** contains twelve carboxylic acid groups. In basic media, the carboxylic groups are present in their deprotonated form, affording carboxylates **2** and **3**. Hence, they can be considered as excellent building blocks for LbL assemblies through electrostatic interactions, as shown in the next section. The synthesis of **6** starts from *tert*-butyl-2-(4-formylphenoxy)acetate (**4**) and pyrrole (Scheme 2). Benzaldehyde **4** was synthesized from 4-hydroxybenzaldeyde and *tert*-butyl 2-(4-formylphenoxy)acetate according to a procedure developed by McKillop et al.[29] Under modified Lindsey conditions,[30] the 10,15,20-(*tert*-butyl-2-phenoxyacetato)-porphyrin **5** is obtained

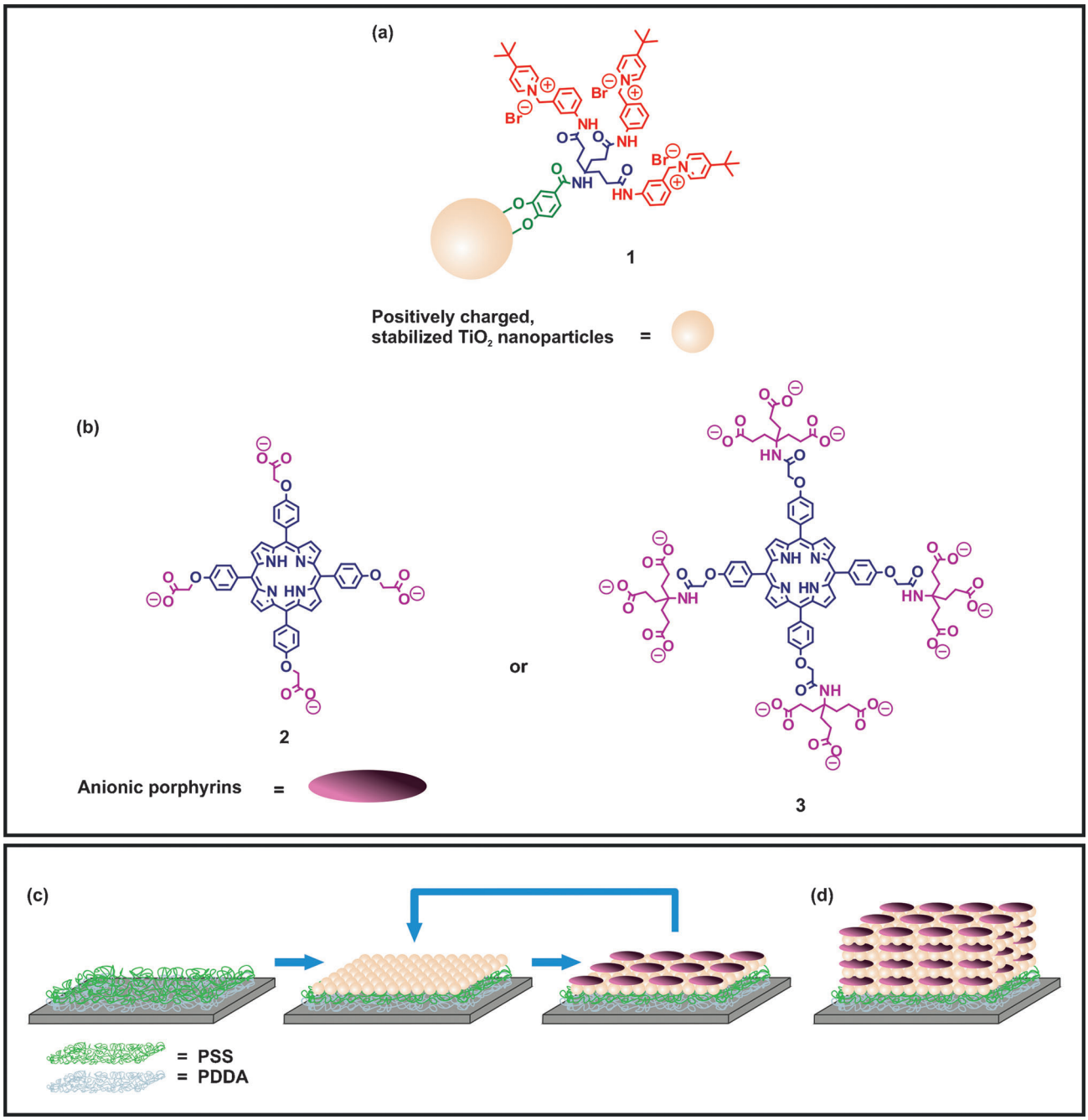

Scheme 1. a) Schematic representation of P25-TiO_2 NPs functionalized with **1**. b) Negatively charged porphyrins **2** and **3**. c) Schematic representation of the corresponding LbL assembly process. d) Representation of the resulting multilayer architectures.

as a purple powder. Subsequent treatment with formic acid at 25 °C leads quantitatively to the desired 5,10,15,20-(phenoxy-acetic acid)-porphyrin **6**. Under modified Steglich conditions,[31] **6** was coupled with the first-generation Newkome-Dendrimer,[32] DCC, and HOBT in DMF to yield 5,10,15,20-(di-*tert*-butyl-4-(3-(*tert*-butoxy)-3-oxopropyl)-4-(2-phenoxy-acetamido)heptanedionato)-porphyrin **7** in 79%. Further treatment of **7** with formic acid at 25 °C afforded quantitatively the second target porphyrin, 5,10,15,20-(4-(2-ethoxycarbonyl)-4-(2-phenoxyacetamido)heptanedioic acid)-porphyrin **8**. All products and intermediates were characterized by ^{1}H-, and ^{13}C NMR as well as HRMS spectroscopy (for details see the Experimental Section).

Owing to the large number of carboxylic acid groups, **6** and **8** are more or less insoluble in organic solvents and only poorly soluble in water or ethanol at neutral pH. To circumvent this, basic media of pH > 7 were utilized to guarantee complete deprotonation of all carboxylic acid groups. Here, aqueous TRIS buffer solutions represent appropriate solvents.

In Figure 1, the absorption and fluorescence spectra of 2.1 μM tris(hydroxymethyl) aminomethane (TRIS) buffered solutions (pH 9) of **6** and **8** are presented.

The absorption spectra of **6** and **8** reveal sharp Soret band absorptions at 424 nm and four Q-band absorptions at 520, 560, 599, and 641 nm. The shape of the Soret band is com-

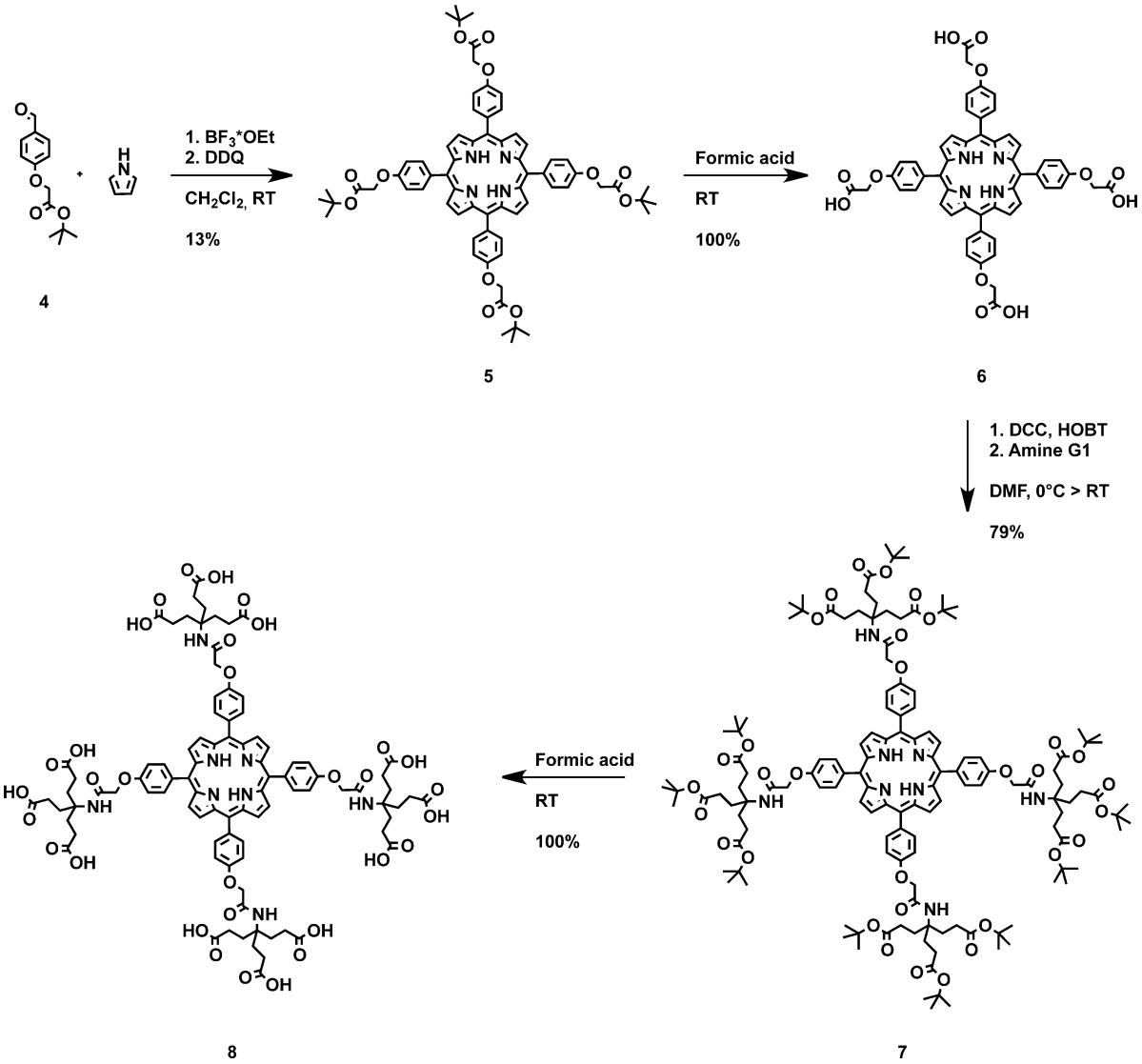

Scheme 2. Schematic representation of the synthesis of 5,10,15,20-(phenoxyacetic acid)-porphyrin (**6**) and 5,10,15,20-(4-(2-ethoxycarbonyl)-4-(2-phenoxyacetamido)heptanedioic acid)-porphyrin (**8**).

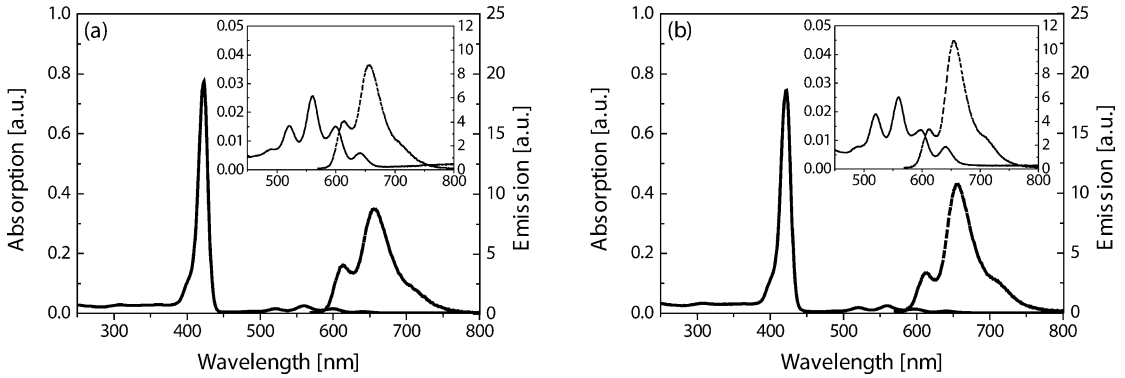

Figure 1. Absorption (solid) and fluorescence (dashed) spectra of 2.1 μM TRIS buffer solutions (pH 9) of **6** (a) and **8** (b).

monly observed in symmetrical porphyrins bearing bulky groups, which hamper aggregation in solution. The latter is also reflected in the high molar extinction coefficients of 3.40×10^5 and $3.17\times10^5\,L\,mol\,cm^{-1}$ for **6** and **8**, respectively. This points to weakly or non-aggregated species as a result of the higher solubility promoted by the carboxylic acid groups. The excited-state characteristics of **6** and **8** were determined by fluorescence spectroscopy in TRIS buffer solutions. As illustrat-

ed in Figure 1, upon excitation at 550 nm, broad fluorescence bands evolved, centered at 614 and 656 nm for **6** and 611 and 654 nm for **8**. Compounds **6** and **8** feature fluorescence quantum yields of 0.12 and 0.14, respectively.

Preparation and characterization of positively functionalized TiO_2 nanoparticles

The positively charged dendron 1,1′-((((4-(3-((3-((4-(*tert*-butyl)-pyridin-1-ium-1-yl)methyl)phenyl)amino)-3-oxopropyl)-4-(3,4-dihydroxybenzamido)heptanedioyl)bis(azanediyl))bis(3,1-phenylene))bis(methylene))bis(4-(*tert*-butyl)pyridin-1-ium) (**1**) was prepared following the procedure that we published previously.[28] In the current work, **1** was used for the first time for the surface functionalization of TiO_2 NPs.

For the formation of stable suspensions of positively charged nanoparticles (Scheme 3), P-25 TiO_2 NPs were functionalized with **1** by mixing an ethanolic suspension of the nanoparticles with an ethanolic solution of **1**, followed by sonication for 50 min at room temperature (for more details see Experimental Section).

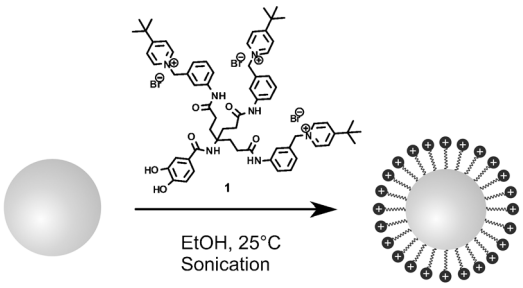

Scheme 3. Schematic representation of the functionalization of TiO_2 nanoparticles with **1**.

For the determination of the required amount of **1** to obtain colloidal stable suspensions, different aliquots of **1** were mixed with the same amount of TiO_2 NPs, keeping the overall volume of ethanol constant. The colloidal properties of pristine TiO_2 NP suspensions were used as a reference. In past works, we calculated the average surface area of **1** to be 2.32 nm^2.[28] Nitrogen adsorption experiments showed that the used P-25 TiO_2 NPs feature a surface area of 51.0 $m^2 g^{-1}$. As a consequence, a monolayer formation of **1** on the NP surface should be obtained upon binding of 0.37×10^{-7} mol mg^{-1} of **1** to the surface. In this study, ethanolic TiO_2 NP suspensions containing different concentrations of **1**, within the range 0.25×10^{-7} mol mg^{-1} (**T6**) to 16.27×10^{-7} mol mg^{-1} (**T1**), were tested. An excess of 0.37×10^{-7} mol mg^{-1}, which corresponds to the theoretically necessary amount for a monolayer formation of **1**, was used to study the equilibrium adsorption and to determine the concentration of **1** to obtain complete surface coverage. For the functionalization, the overall TiO_2 concentration was 2.08 mg mL^{-1}. After functionalization, all suspensions were washed with ethanol to remove any non-bound surfactants (for details see the Experimental Section). Immediately after mixing, a rapid color change from white to light yellow sets in for the NP suspensions. Moreover, the intensity of the color increases from **T1** to **T6**, whereas reference **T7** remains white, as shown in Figure 2. A color change of TiO_2 upon mixing with catechol was already observed by Moser et al.[33] In our case, no significant changes in the absorption spectra of the functionalized TiO_2 NPs were detected.

Figure 2. TiO_2 NPs functionalized with different amounts of **1**. From left to right: 16.27×10^{-7} mol mg^{-1} (**T1**), 4.07×10^{-7} mol mg^{-1} (**T2**), 2.03×10^{-7} mol mg^{-1} (**T3**), 1.02×10^{-7} mol mg^{-1} (**T4**), 0.51×10^{-7} mol mg^{-1} (**T5**), 0.25×10^{-7} mol mg^{-1} (**T6**), and 0 mol mg^{-1} (**T7**).

Next, we compared the colloidal behavior of TiO_2 NPs with 4.07×10^{-7} mol mg^{-1} (**T2**) with the reference NP suspension (**T7**) at a concentration of 29×10^{-3} mg mL^{-1} (Figure 3).

Although **T7** and **T2** form slightly turbid suspensions upon sonication, NPs in reference **T7** sediment after 24 h, whereas the functionalized TiO_2 nanoparticles **T2** remain stable in suspension (see Figure 3 b). This is a first proof that agglomeration of TiO_2 NPs is suppressed and that stable suspensions are obtained upon functionalization with **1**.

Thermogravimetric analysis (TGA) was performed to gain information about the equilibrium adsorption of **1** on the TiO_2

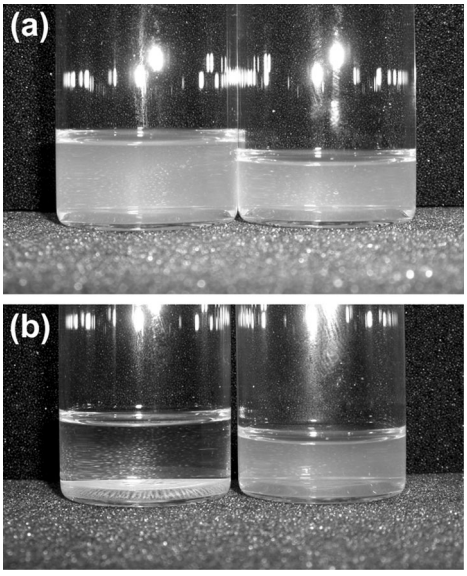

Figure 3. Ethanolic suspensions of pristine TiO_2 NPs **T7** (left) and functionalized TiO_2 NPs **T2** (right) with a concentration of 29×10^{-3} mg mL^{-1}, directly after sonication (a) and after aging for 24 h (b).

surface. The difference in mass losses between functionalized and pristine TiO_2 NPs allows the determination of the exact amount of chemisorbed catechol. The TiO_2 NPs were functionalized with different amounts of **1**, so an adsorption isotherm could be derived from the TGA data.

Figure 4 shows that upon functionalization of TiO_2 NPs with different amounts of **1**, ranging from 0.25×10^{-7} mol mg^{-1} (**T1**)

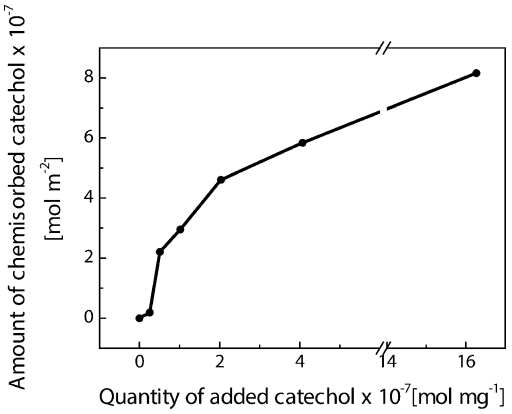

Figure 4. Adsorption isotherm for the functionalization of TiO_2 NPs with **1** as a function of the added amount of **1** with an overall TiO_2 concentration of 2.08 mg mL^{-1}.

to 16.27×10^{-7} mol mg^{-1} (**T6**), the adsorption increases. The exact values for all the different concentrations are summarized in Table 1. The highest loading of 8.16×10^{-7} mol m^{-2} was

Table 1. Chemisorbed amount of **1** on TiO_2 NPs depending on the quantity of **1** added for the functionalization.

Sample	Quantity of added catechol [mol mg^{-1}]	Amount of chemisorbed catechol [mol m^{-2}]	Number of adsorbed molecules per m^2
T1	16.27×10^{-7}	8.16×10^{-7}	4.9×10^{17}
T2	4.07×10^{-7}	5.84×10^{-7}	3.5×10^{17}
T3	2.03×10^{-7}	4.61×10^{-7}	2.8×10^{17}
T4	1.02×10^{-7}	2.95×10^{-7}	1.8×10^{17}
T5	0.51×10^{-7}	2.21×10^{-7}	1.3×10^{17}
T6	0.25×10^{-7}	1.87×10^{-8}	0.1×10^{17}

obtained upon functionalization of NPs with 16.27×10^{-7} mol mg^{-1} (**T1**) in an overall TiO_2 concentration of 2.08 mg mL^{-1}. Taking the theoretically calculated maximum amount of **1** into account, this corresponds to 100% coverage of the surface, and as a consequence, to monolayer formation.

Next, the zeta potential and hydrodynamic diameter were measured to obtain additional information about the colloidal stability of the functionalized TiO_2 NPs. In general, the zeta potential assists in drawing conclusions about the colloidal stability of NPs.[34] For example, high negative or positive values correspond to high charge densities on the particle surface, and, in turn, to stable suspensions owing to electrostatic repulsions. Low potentials, on the contrary, indicate moderate or low surface charge densities. In general, this may result in aggregation

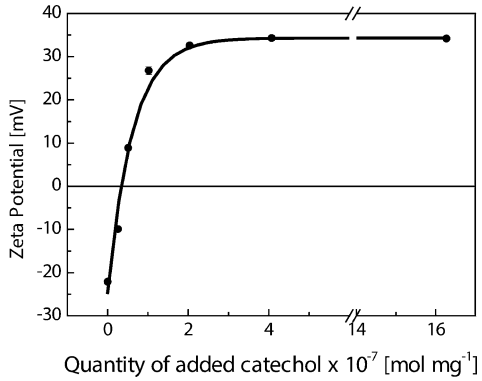

Figure 5. Zeta potential values of ethanolic suspensions as a function of different quantities of **1** added to TiO_2 NPs.

owing to the absence of repulsive forces.[23a] If dispersed in liquids, TiO_2 NPs may have OH-terminated surfaces, which are deprotonated in protic solvents such as water or ethanol, resulting in negative zeta potentials. Figure 5 shows the zeta potentials of ethanolic suspensions of TiO_2 NPs as a function of the quantity of **1**. Overall, the zeta potentials increase with increasing amount of **1**. Nonfunctionalized particles **T7** display a zeta potential of -22.1 ± 0.53 mV. Samples treated only with small quantities of **1** show increased, but low, zeta potential values. For **T6** and **T5**, we recorded -9.9 ± 0.23 and 8.9 ± 0.23 mV, respectively, which indicate the low colloidal stabilities of the suspensions. Furthermore, the zeta potential rises to $+26.8\pm0.91$ (**T4**), $+32.6\pm0.59$ (**T3**), $+34.3\pm0.60$ (**T2**), and $+34.2\pm0.03$ mV (**T1**). With regard to the highly negative zeta potential values of the nonfunctionalized TiO_2 NPs, we also considered electrostatic interactions of the positively charged catechol with the NP surface. Taking into account that highly positive values for the zeta potential are obtained for suspensions **T1** to **T4**, even after three washing steps with pure ethanol, pure electrostatic coordination are negligible. A strong covalent binding of the catechol to the NP surface is approved, because in the case of pure electrostatic coordination of **1** to the surface, zeta potential values would decrease again after washing of the NPs.

The presence of larger quantities of **1** leads to higher values of the zeta potential and to higher stabilities of the suspensions owing to increased electrostatic repulsions between NPs. From the zeta potential measurements we derive that stable ethanolic suspensions were obtained not only for NPs featuring a monolayer of **1** (**T1**), but also for NPs functionalized with 4.07×10^{-7} (**T2**), 2.03×10^{-7} (**T3**), and 1.02×10^{-7} mol mg^{-1} (**T4**).

The stability of the suspensions was evaluated from the particle size distributions found through dynamic light scattering at different time delays. To this end, measurements were taken directly after sonication (time = 0 h) and after ageing for 0.5, 2, and 24 h. Figure 6 shows the average hydrodynamic diameter of the TiO_2 NPs in ethanol with time.

Directly after sonication, all the suspensions, with the exception of **T6**, feature hydrodynamic diameters similar to that of unmodified TiO_2. **T6** features slightly higher values for the hydrodynamic diameter and size distribution from the beginning,

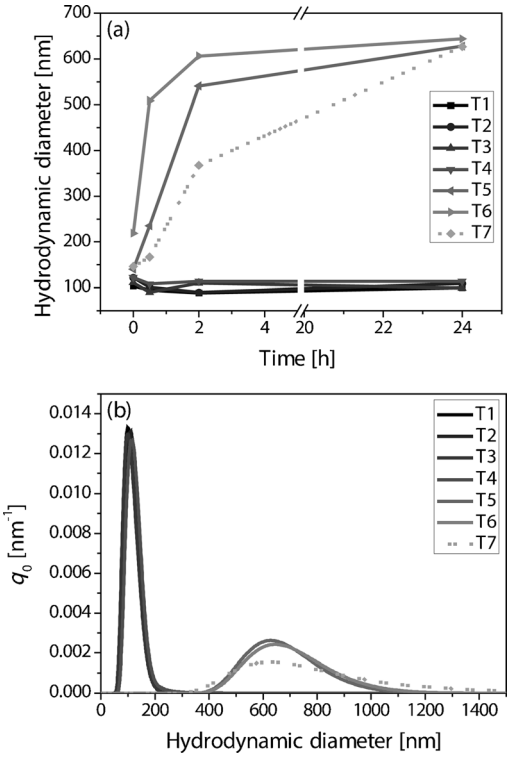

Figure 6. a) Hydrodynamic diameter of TiO_2 NPs **T1** (■, solid), **T2** (●, solid), **T3** (▲, solid), **T4** (▼, solid), **T5** (◀, solid), **T6** (▶, solid), and **T7** (◆, dotted) as a function of time, and b) particle size distributions after aging of TiO_2 suspensions **T1**–**T7** for 24 h.

which gives reason to assume that nanoparticles functionalized under these specific conditions form unstable suspensions. During ageing at 25 °C, poorly functionalized NPs form agglomerates (**T5** and **T6**), whereas the particle size distributions of successfully functionalized TiO_2 NPs remain unchanged (**T1** to **T4**). These observations are in good agreement with the zeta potential measurements. On one hand, TiO_2 nanoparticles of **T1** to **T4** carry a sufficient number of positive charges, introduced by functionalization with **1**, to form stable colloidal suspensions. On the other hand, **T5** and **T6** seem to agglomerate with time owing to insufficient functionalization and a lack of electrostatic repulsions. **T7** agglomerates as no stabilizing surfactants are present. Comparing these results with those from TGA measurements, we observe that complete monolayer formation on the particle surface is not necessarily required to obtain stable nanoparticle suspensions. Monolayer formation was achieved upon functionalization of the NPs with 16.27×10^{-7} mol mg^{-1} (**T1**) of **1**. However, we derived from zeta potential and DLS measurements that nanoparticles functionalized with 1.02×10^{-7} mol mg^{-1} (**T4**) already form stable ethanolic suspensions. Thus, NPs carrying 2.95×10^{-7} mol m^{-2} of **1** on the surface (**T4**), which corresponds to 41% of the amount required for the formation of a monolayer, already form stable ethanolic suspensions.

To round off the characterization of catechol-functionalized TiO_2 NPs, scanning electron microscopy (SEM) investigations with thin films prepared by drop-casting of ethanolic TiO_2 NP suspensions were performed. Figure 7 displays SEM images of

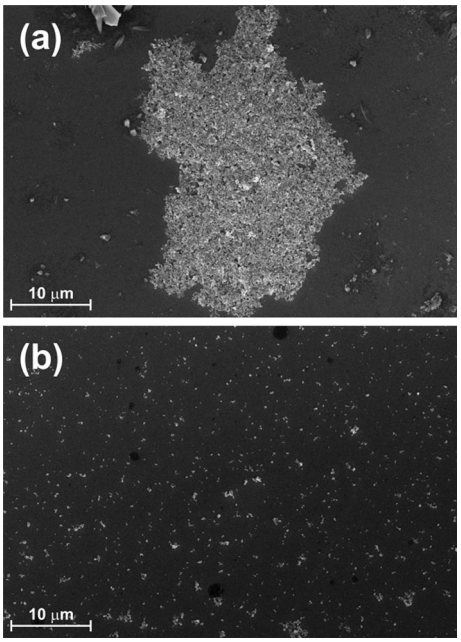

Figure 7. SEM images of a) pristine TiO_2 NPs and b) TiO_2 NPs functionalized with **1**.

films prepared with pristine and functionalized TiO_2 nanoparticles. TiO_2 NPs were functionalized with 1.84×10^{-7} mol mg^{-1} (**T8**), which is, according to the previously discussed experiments, a concentration sufficient to ensure the successful functionalization of TiO_2 NPs.

Importantly, the SEM images confirm the presence of TiO_2 NPs. Whereas pristine TiO_2 NPs form large agglomerates on silica wafers during drying, a lack of the latter is observed for any of the functionalized TiO_2 NPs. In fact, the latter are best described as small islands, which are homogenously distributed throughout the wafer. Again, we take this as support for the successful stabilization of TiO_2 NPs in suspension (Figure 7).

Formation of layer-by-layer assemblies of catechol-functionalized TiO_2 nanoparticles and porphyrins

Having accomplished both, the successful functionalization of TiO_2 NPs to obtain stable ethanolic suspensions of positively charged NPs and the synthesis of negatively charged porphyrins, the construction of LbL assemblies was investigated. Here, we constructed LbL assemblies consisting of positively charged TiO_2 NPs and negatively charged porphyrins on three different substrates, namely soda-lime-glass, silicon wafers, and indium tin oxide (ITO) electrodes. The assembly formation was performed using a 10^{-3} M ethanolic suspension of functionalized TiO_2 NPs **T8** and 10^{-3} M solutions of porphyrins **2** and **3** in aqueous TRIS buffer solution (pH 9). To monitor the LbL formation, we initially utilized soda-lime-glass and silicon wafer substrates, which allow the performance of absorption, profilometry, and SEM studies. Indium tin oxide (ITO) electrodes were used to perform device assays. Regardless of the type of substrate, the LbL deposition started with the deposition of a thin layer of positively charged poly-(diallyl-dimethylammonium)

($PDDA^+$) and/or negatively charged poly-(sodium-4-styrenesulfonat) (PSS^-). To this end, the substrate surface was modified with either positive or negative charges that allow the preparation of different films, namely $[PDDA^+\text{-}PSS^-]_xPDDA^+\text{-}[porphyrin\text{-}TiO_2]_x$ and $[PDDA^+\text{-}PSS^-]_x\text{-}[TiO_2\text{-}porphyrin]_x$, in which x is the number of sandwich layers. As an example, Figure 8 shows in detail the procedure for the preparation of

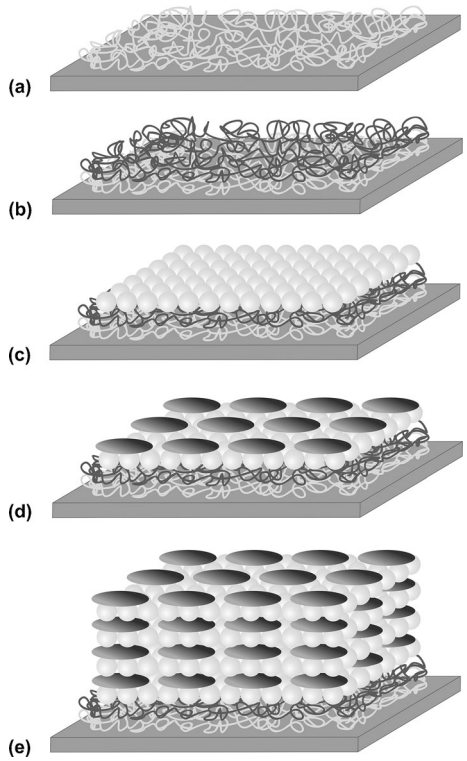

Figure 8. Formation of layer-by-layer assemblies. a) Deposition of $PDDA^+$, b) deposition of PSS^-, c) deposition of positively charged TiO_2 NPs, d) deposition of negatively charged porphyrins, e) multiple LbL assemblies of porphyrins and TiO_2 NPs.

the LbL films. First, a layer of $PDDA^+$ was deposited onto the surface through dip-coating for 10 min followed by washing with a mixture of ethanol/water 1:1 (v/v), and drying with a stream of air. This procedure resulted in substrates that were covered with positively charged hydrophilic surfaces. Secondly, the same procedure was followed to deposit PSS^- onto the $PDDA^+$-covered substrate, to obtain a negatively charged hydrophilic surface. The first two steps were repeated up to four times to ensure a thin homogenous layer of around 30 nm. Thirdly, alternate depositions of positively functionalized TiO_2 NPs and negatively charge porphyrins achieved by dipping the modified substrates for 10 min each into the corresponding suspensions enabled the formation of multilayer assemblies. The application of these deposition times is important, as stable and constant layer growth is achieved only after a certain time period.[35]

In a first approach, the LbL growth with **T8** and porphyrins **2** and **3**, respectively, was monitored by UV/Vis spectroscopy. Therefore, LbL assemblies have been built up on soda-lime-glass substrates with a polymer base consisting of $[PDDA^+\text{-}PSS^-]_4\text{-}PDDA^+$.[36] Absorption spectra were recorded after the deposition of each porphyrin layer. On one hand, strong Soret- and weaker Q-band absorptions are discernible at around 430 nm and in the 520–660 nm range, respectively. On the other hand, a broad band at around 320 nm, which is ascribed to the TiO_2 NPs, is also clearly noted. At first glance, the intensities of all of these absorption bands increase linearly (Figure 9). This finding confirms successful LbL deposition.

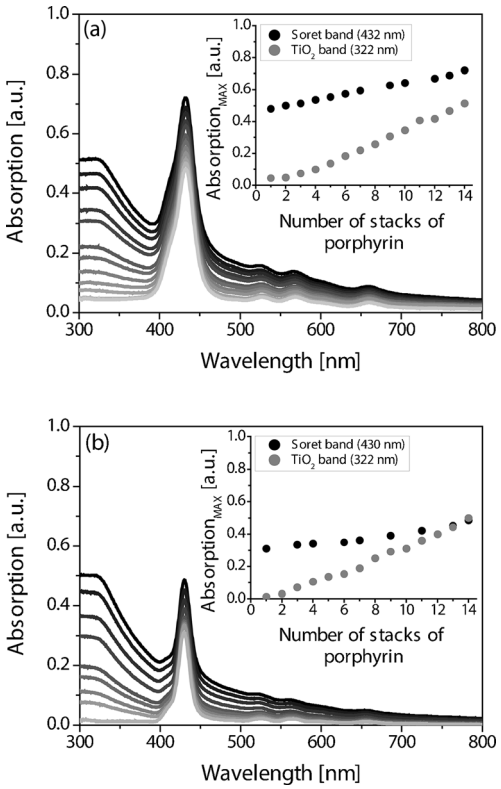

Figure 9. Absorption spectra of LbL assemblies of a) **T8** and **2** or b) **T8** and **3**. The inset describes the dependence of the maxima of the Soret band of the porphyrins and of the TiO_2 band on the number of stacks of porphyrin deposited on the substrate.

However, a closer look reveals subtle differences. For example, a direct comparison of the absorption spectra reveals that utilizing porphyrin **3** for the buildup of LbL assemblies results in a smaller increase in the Soret-band absorption (17.6%) compared with those being built up with porphyrin **2** (24.0%). In contrast, the intensity of the band ascribed to the TiO_2 nanoparticles increases by more or less equal values upon utilization of porphyrin **2** (47.1%) or **3** (48.4%). Considering that both porphyrins feature similar extinction coefficients, that is, 3.40×10^5 (**2**) versus $3.17\times10^5\,L\,mol\,cm^{-1}$ (**3**), we infer that differences in the steric hindrance and the number of charges at the porphyrin are responsible for the slightly different amounts of the porphyrins. Different quantities of porphyrins **2** and **3** adsorbed on the substrate provide therewith the same overall density of negative charges; hence, the same quantities of functionalized TiO_2 NPs are adsorbed.

Regardless of the type of porphyrin, the film thicknesses of the assemblies, which were prepared on silicon wafers, were probed by combining ellipsometry and profilometry measurements. The former indicates that each porphyrin layer deposition increases the overall thickness by about 0.3–0.6 nm. The latter implies that each deposition of functionalized TiO_2 NPs increases the thickness by around 30–50 nm. Notably, we monitor the sequential increase in the layer thickness by combining both techniques to obtain a linear relationship that corroborates the absorption measurements (Figure 10).

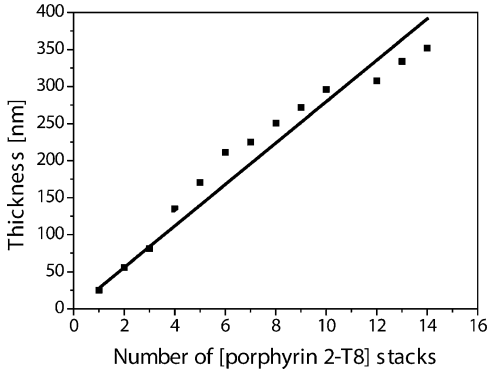

Figure 10. Thickness of the LbL assemblies on silicon wafer as a function of [porphyrin **2**-**T8**] stacks.

For confirmation of the notion of controlled two-dimensional film growth, SEM images of the assemblies prepared on silicon wafers were obtained (Figure 11). SEM images were recorded after one, three, and six deposition cycles. A good coverage with uniformly distributed TiO_2 NPs on the substrate was already obtained after six deposition cycles, indicating the successful control of the homogeneous LbL deposition as a means to integrate functionalized TiO_2 NPs and anionic porphyrins.

Photoelectrochemical cell fabrication

Encouraged by the features of the LbL assemblies, we turned to the fabrication of photoelectrochemical cells with photoactive ITO electrodes modified by sequential LbL deposition of the functionalized TiO_2 NPs and both porphyrins. Importantly, the assemblies prepared on ITO substrates showed strong fluorescence quenching of both porphyrins upon 420 nm excitation, indicating a qualitative electron and/or energy transfer from the porphyrin to the TiO_2 NPs (Figure 12).

As reference electrodes, the porphyrins were replaced with PSS^- to give ITO-[$PDDA^+$-PSS^-]-[**T8**-PSS^-]$_x$. To complete the devices we utilized polysulfide electrolytes (i.e., equimolar 3 M Na_2S/S/NaOH) and Cu_2S-based counter electrodes (for more details see Experimental Section).

As shown in Figure 13, assemblies prepared with porphyrins **2** and **3** reveal promising and stable photoresponse profiles during several "on-off" cycles of illumination under AM 1.5 conditions. In line with the absorption features, the photocurrents for **2** and **3** in the "on-off" experiments are rather similar. The

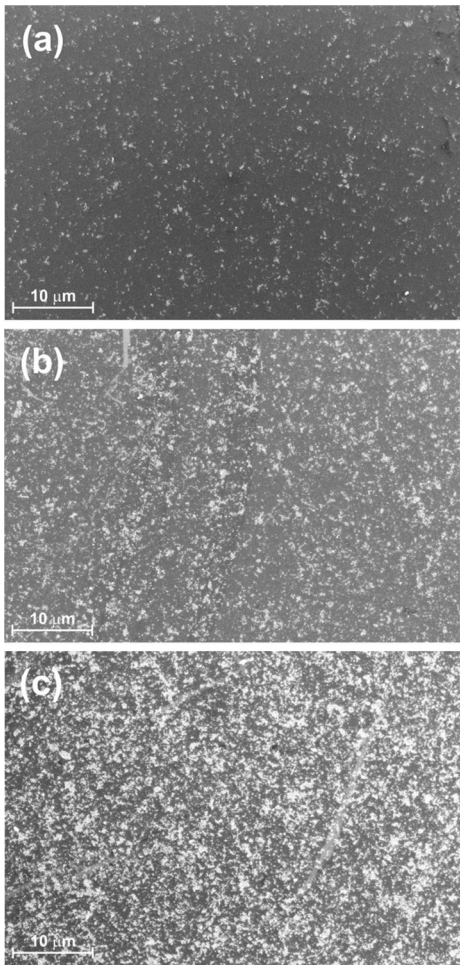

Figure 11. SEM images of a silicon wafers coated with a) [$PDDA^+$-PSS^-]$_4$-$PDDA^+$-[**2**-**T8**]$_1$, b) [$PDDA^+$-PSS^-]$_4$-$PDDA^+$-[**2**-**T8**]$_3$, and c) [$PDDA^+$-PSS^-]$_4$-$PDDA^+$-[**2**-**T8**]$_6$.

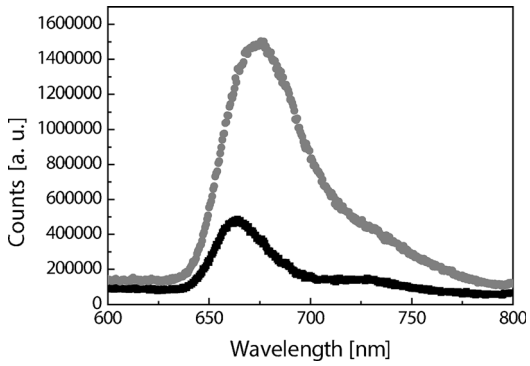

Figure 12. Fluorescence spectra of ITO-[$PDDA^+$-PSS^-]$_4$-$PDDA^+$-[**2**] (gray) and ITO-[$PDDA^+$-PSS^-]$_4$-$PDDA^+$-[**2**-**T8**] (black) films at 420 nm excitation.

aforementioned trends were validated in complementary *I–V* measurements under AM 1.5 conditions. On one hand, maximum short-circuit current densities of around 25 μA cm^{-2} were derived for both assemblies, featuring, however, only a single stack layer, that is, ITO-[$PDDA^+$-PSS^-]$_4$-$PDDA^+$-[porphyrin-**T8**]$_1$. The main differences between the assemblies are seen in the

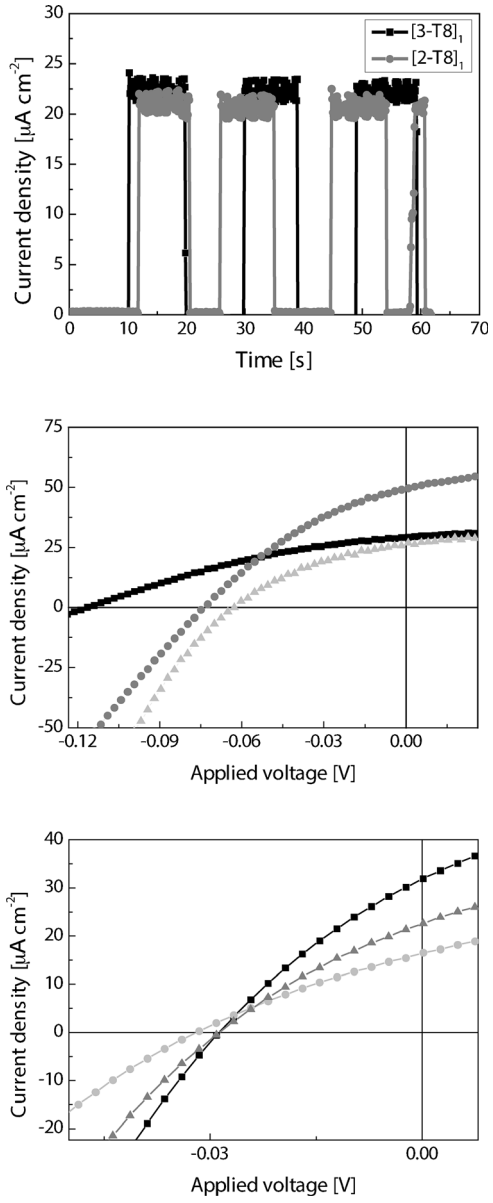

Figure 13. Top: Photocurrent generated under "on-off" illumination cycles for photoelectrodes ITO-[PDDA$^+$-PSS$^-$]$_4$-PDDA$^+$-[**3**/**T8**]$_1$ (black) and ITO-[PDDA$^+$-PSS$^-$]$_4$-PDDA$^+$-[**2**-**T8**]$_1$ (gray). Center: Photocurrent–voltage characteristics of ITO-[PDDA$^+$-PSS$^-$]$_4$-PDDA$^+$-[**2**-**T8**]$_x$ photoelectrodes with increasing number of [**2**-**T8**] sandwich layers [1 (black), 3 (gray), and 6 (light gray)] under AM 1.5 conditions. Bottom: Photocurrent–voltage characteristics of ITO-[PDDA$^+$-PSS$^-$]$_4$-PDDA$^+$-[**3**-**T8**]$_x$ photoelectrodes with increasing number of [**3**-**T8**] sandwich layers [1 (black), 3 (gray), and 6 (light gray)] under AM 1.5 conditions.

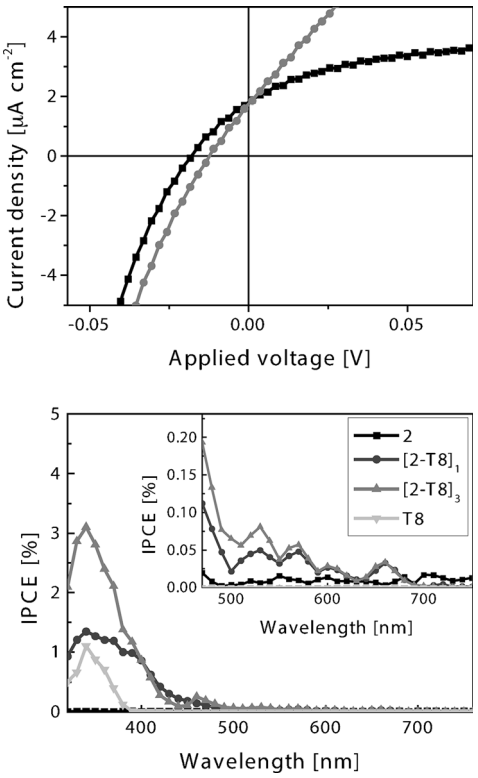

Figure 14. Top: Photocurrent–voltage characteristics of ITO-[PDDA$^+$-PSS$^-$]$_4$-[**T8**-PSS$^-$]$_x$ photoelectrodes with increasing number of [**T8**-PSS$^-$] sandwich layers [1 (black) and 3 (gray)] under AM 1.5 conditions. Bottom: IPCE spectra of ITO-[PDDA$^+$-PSS$^-$]$_4$-PDDA$^+$-**2** (■, black), ITO-[PDDA$^+$-PSS$^-$]$_4$-**T8** (▼, light gray), ITO-[PDDA$^+$-PSS$^-$]$_4$-PDDA$^+$-[**2**-**T8**]$_1$ (●, dark gray), and ITO-[PDDA$^+$-PSS$^-$]$_4$-PDDA$^+$-[**2**-**T8**]$_3$ (▲, gray) photoelectrodes under AM 1.5 conditions. Inset graph is a magnification to show the contribution from the Q-bands.

open-circuit voltages, which are 0.12 and 0.03 V for assemblies with **2** and **3**, respectively. As a consequence, photoelectrodes prepared with **2** feature efficiencies four times higher than those prepared with **3**: 1×10^{-3} versus 2.5×10^{-4}%. On the other hand, the increase in the number of sandwich layers has different impacts in the two assemblies. For **2**, increasing the number of layers to three enhances the photocurrent values from 25 to 50 μA cm^{-2}, and the open-circuit voltage is reduced from 0.12 to 0.07 V. A further increase in the number of layers leads to a significant reduction in both the photocurrent and the open-circuit voltage parameters (Figure 13). For **3**, the device performance is reduced dramatically upon increasing the number of layers. Such behavior is ascribable to the thickness of the photoelectrode, which increases after each sandwich layer deposition to reach a value of around 400 nm. Although light-harvesting by the electrodes is enhanced with each deposition, the loss of open-circuit voltage with thickness implies that the electron transport and electron collection at the electrode are interrupted because of recombination processes with the electrolyte. In fact, the overall photogenerated currents decrease.

Figure 14 reveals that measurements under monochromatic illumination to determine the incident photon conversion efficiency (IPCE) spectrum show a good resemblance to the absorption spectrum. From this, we hypothesize that the photosensitizing attributes of both porphyrins are the inception for electron injection into functionalized TiO_2 NPs. To corroborate this hypothesis, we prepared devices lacking any porphyrins, that is, ITO-[PDDA$^+$-PSS$^-$]-[**T8**-PSS$^-$]$_x$ devices. The lack of appreciable photocurrents (<4 μA cm^{-2}) upon increasing the number of [TiO_2-PSS$^-$] sandwich layers clearly confirmed that the porphyrins are responsible for the photogenerated currents (Figure 14).

Conclusion

P25-TiO_2 NPs were successfully functionalized with N1,N7-bis(3-(4-*tert*-butyl-pyridium-methyl)phenyl)-4-(3-(3-(4-*tert*-butyl-pyridinium-methyl)phenylamino)-3-oxopropyl)-4-(3,4-dihydroxybenzamido)heptanediamide tribromide (**1**). From zeta potential and DLS measurements we derived that stable colloidal suspensions are realized if a minimum concentration of 1.02×10^{-7} mol mg^{-1} (**T4**) is used for the NP functionalization. In particular, strongly positive values for the zeta potential and small average hydrodynamic diameters were determined. TGA measurements showed that by functionalizing TiO_2 NPs with concentrations equal to 1.02×10^{-7} mol mg^{-1}, 2.65×10^{-7} mol m^{-2} of **1** is adsorbed on their surface. This corresponds to 41% of the amount needed for monolayer formation on the NP surface. The maximum coverage of 8.16×10^{-4} mmol m^{-2}, which corresponds to the formation of a monolayer, was obtained upon functionalization with 16.27×10^{-7} mol mg^{-1} (**T1**) and an overall TiO_2 concentration of 2.08 mg mL^{-1}. Therefore, we conclude that at least 41% of the surface needs to be covered with **1** to achieve colloidal stability of the TiO_2 NPs.

Furthermore, the successful synthesis of two porphyrin derivatives, 5,10,15,20-(phenoxyacetic acid)-porphyrin (**6**) and 5,10,15,20-(4-(2-ethoxycarbonyl)-4-(2-phenoxyacetamido)heptanedioic acid)-porphyrin (**8**) was presented. Both porphyrins feature anionic carboxylates under basic conditions, which make them excellent building blocks for the formation of layer-by-layer assemblies with TiO_2 NPs **1** through electrostatic interactions. Layer-by-layer assemblies were built up on three different substrates. Investigation of layer-by-layer assemblies of functionalized TiO_2 NPs **1** and porphyrins **2** or **3** by UV/Vis spectroscopy showed that the quantity of adsorbed porphyrin depends on their structure. SEM studies confirmed the formation of homogeneous TiO_2 layers after six deposition cycles, and ellipsometry and profilometry assays also indicated a linear increase in the thickness up to a value of 400 nm upon the deposition of 14 sandwich layers. Finally, we demonstrated the performance of photoelectrodes prepared with both LbL hybrids, which showed stable and repeatable photocurrent generation during several "on-off" cycles of illumination with monochromatic incident photo-to-current conversion efficiencies of around 3%.

Experimental Section

Chemicals and instruments

All chemicals were purchased from chemical suppliers and used without further purification. All analytical reagent-grade solvents were purified by distillation.

Average hydrodynamic diameters and zeta potentials of nanoparticles in ethanolic dispersions were measured with a Zetasizer Nano (Malvern Instruments Ltd. UK) dynamic light scattering (DLS) analyzer. Intensity distributions were recorded for TiO_2 nanoparticle suspensions in ethanol with a particle concentration of 16×10^{-3} mg mL^{-1} at 25 °C. The suspensions were sonicated for 1 h at 25 °C (time = 0).

Thermogravimetric measurements of dried powders were performed on a TGA Q50 device (TA Instruments) in ramp regime (5 °C min^{-1}) under a nitrogen flow over the temperature range 20–950 °C. The amounts of chemisorbed compounds were calculated from the weight loss in the temperature range 100–845.8 °C.

Nitrogen sorption experiments at liquid nitrogen temperature were performed with a volumetric gas sorption analyzer (Nova4200e; Quantachrome, Odelzhausen, Germany). Degassing under vacuum conditions was performed for 2 h at 120 °C. Mass specific surface areas (S_m) were evaluated in a p/p_0 range from 0.02 to 0.35 according to the Brunauer–Emmett–Teller (BET) theory. Mesopore volumes were calculated from desorption data using the Barrett–Joyner–Halenda (BJH) model; relative pressures below 0.35 were omitted for the calculations.

Scanning electron microscopy images were recorded with a field emission scanning electron microscope (ULTRA 55, Carl Zeiss NTS GmbH, Germany) at an operating voltage of 10 kV using an in-lens secondary electron detector. TiO_2 nanoparticles were functionalized with 1.84×10^{-7} mol mg^{-1}. The samples were prepared by drop-casting of ethanolic suspensions on silicon wafers.

Adsorption spectra were recorded with Varian Cary 5000 (characterization of porphyrins) and Shimadzu UV-3102 PC (characterization of layer-by-layer assemblies) instruments.

Profilometry measurements were performed with a DektakXT on silica wafers and ITO for the study of film formation and device fabrication, respectively. We used a Stylus tip of 12.5 mm with a force of 3 mg and a resolution of 0.66 mm/pt.

The ellipsometric measurements were performed with a spectroscopic ellipsometer HORIBA Smart SE on a silicon wafer using a stable laser power of 12 mW and an angle of 70°. For the fitting of the characteristics we used the data of the tetraphenylzincporphyrin included in the database of the program.

Emission spectra were recorded with a Shimadzu RF-5301 PC instrument.

Mass spectra were recorded with Shimadzu AXIMA Confidence (MALDI-TOF, matrices: sinapinic acid SIN, 2,5-dihydroxybenzoic acid DHB) and Bruker Esquire 6000 (ESI-QIT) instruments.

NMR spectra were recorded with Bruker Avance 300 (300 MHz), Avance 400 (400 MHz), and Jeol EX 400 (400 MHz) spectrometers. Chemical shifts are given in ppm relative to TMS. The resonance multiplicities are indicated as s (singlet), d (doublet), and t (triplet), and broad resonances are indicated as bs.

Synthesis of anionic porphyrins 5,10,15,20-(phenoxyacetic acid)-porphyrin (2) and 5,10,15,20-(4-(2-ethoxycarbonyl)-4-(2-phenoxyacetamido)heptanedioic acid)-porphyrin (3)

5,10,15,20-(*tert*-Butyl-2-phenoxyacetato)-porphyrin (5): *tert*-Butyl-2-(4-formylphenoxy)acetate (3 g; 12.71 mmol) and pyrrole (0.89 mL; 12.71 mmol) were dissolved in CH_2Cl_2 (1.9 L). EtOH (15 mL) and $BF_3{\cdot}OEt_2$ (0.16 mL; 1.27 mmol) were added. The solution was stirred at room temperature for 1.5 h. DDQ (2.16 g; 9.53 mmol) was added and the solution was stirred at room temperature for 3.5 h. Afterwards, the volume of the reaction media was reduced to 400 mL and the solvent was removed on a rotary evaporator. The residual was filtered over a silica plug with CH_2Cl_2 as eluent, followed by further purification through column chromatography over silica with a mixture of CH_2Cl_2/EtOAc (98:2) as eluent. The solvent was removed under reduced pressure on a rotary evaporator and the product was dried under vacuum. Yield: 0.875 g (0.77 mmol), 6%.

^{1}H NMR (400 MHz, 25 °C, $CDCl_3$): $\delta = -2.81$ (bs, 2H, N*H*), 1.59 (s, 36H, CH_3), 4.80 (s, 8H, CH_2), 7.26 (d, $^3J = 8.5$ Hz, 8H, C*H-benz*), 8.10 (d, $^3J = 8.5$ Hz, 8H, C*H-benz*), 8.83 ppm (s, 8H, C*H-pyrr*); ^{13}C NMR (400 MHz, 25 °C, $CDCl_3$): $\delta = 14.48$ (s, 12C, CH_3), 52.38 (s, 4C, CH_2), 68.91 (s, 4C, CCH_3), 99.22 (s, 8C, *C*H-benz), 105.85 (s, 4C, *C-por*), 121.75 (s, 4C, *C*-C-benz), 121.83 (s, 8C, *C*H-benz), 144.14 (s, 4C, *C*-O-benz), 154.48 ppm (s, 4C, $COOCCH_3$); MS (MALDI, sin): *m/z*: 1135 $[M]^+$, 1136 $[M+H]^+$, 1137 $[M+2H]^+$; HRMS (ESI-TOF, MeOH-ACN): *m/z* calcd for $C_{68}H_{70}N_4O_{12}$: 1135.5063 $[M]^+$; found: 1135.5049 $[M]^+$.

5,10,15,20-(Phenoxyacetic acid)-porphyrin (6): 5,10,15,20-(*tert*-Butyl-2-phenoxyacetato)-porphyrin (334 mg; 0.29 mmol) was dissolved in formic acid (25 mL). The solution was stirred for 18 h at room temperature. The formic acid was removed on a rotary evaporator. Subsequently, the product was transferred to toluene and evaporated twice to remove any residual formic acid. The product was finally dried under reduced pressure. Yield: 260 mg (0.28 mmol), 99%.

^{1}H NMR (400 MHz, 25 °C, DMSO): $\delta = -2.91$ (s, 2H, N*H*), 4.97 (s, 8H, CH_2), 7.35 (d, $^3J = 8.4$ Hz, 8H, C*H*-benz), 8.12 (d, $^3J = 8.4$ Hz, 8H, C*H-benz*), 8.84 (s, 8H, C*H-pyrr*), 13.16 ppm (bs, 4H, COO*H*); ^{13}C NMR (400 MHz, 25 °C, DMSO): $\delta = 64.84$ (s, 4C, CH_2), 113.04 (s, 8C, *C*H-benz), 119.57 (s, 4C, *C-por*), 133.94 (s, 4C, *C*-C-*benz*), 135.31 (s, 8C, *C*H-*benz*), 157.73 (s, 4C, *C*-O-*benz*), 170.32 ppm (s, 4C, *C*OOH); MS (MALDI, om): *m/z*: 911 $[M]^+$, 912 $[M+H]^+$, 913 $[M+2H]^+$; HRMS (ESI-TOF, MeOH-THF): *m/z* calcd for $C_{52}H_{38}N_4O_{12}$: 910.248074 $[M]^+$; found: 910.244958 $[M]^+$; calcd for $C_{52}H_{39}N_4O_{12}$: 911.255899 $[M+H]^+$; found: 911.252284 $[M+H]^+$.

5,10,15,20-(Di-*tert*-butyl-4-(3-(*tert*-butoxy)-3-oxopropyl)-4-(2-phenoxyacetamido)heptanedionato)-porphyrin (7): 5,10,15,20-(Phenoxyacetic acid)-porphyrin (140 mg; 0.15 mmol) was dissolved in DMF (25 mL) and the solution was cooled to 0 °C. Di-*tert*-butyl-4-amino-4-(3-(*tert*-butoxy)-3-oxopropyl)heptanedionate (461.32 mg; 1.11 mmol) was added, then DCC (216.37 mg; 1.05 mmol) and HOBT (141.88 mg; 1.05 mmol) were added and the solution was stirred for three days at room temperature. The solvent was removed under reduced pressure on a rotary evaporator and the product was purified through column chromatography over silica with a mixture of CH_2Cl_2 and EtOAc (4:1) as eluent. Yield: 273 mg (0.11 mmol), 79%.

^{1}H NMR (400 MHz, 25 °C, $CDCl_3$): $\delta = -2.79$ (s, 2H, N*H*), 1.44 (s, 108H, C*H3*), 2.14 (t, $^3J = 8.6$ Hz, 24H, CH_2CH_2CO), 2.34 (t, $^3J = 8.6$ Hz, 24H, CH_2CH_2CO), 4.69 (s, 8H, CH_2), 6.84 (s, 4H, CON*H*), 7.34 (d, $^3J = 8.6$ Hz, 8H, C*H-benz*), 8.16 (d, $^3J = 8.6$ Hz, 8H, C*H-benz*), 8.84 ppm (s, 8H, C*H-pyrr*); ^{13}C NMR (400 MHz, 25 °C, $CDCl_3$): $\delta = 28.00$ (s, 36C, CH_3), 29.66 (s, 12C, CH_2CH_2CO), 29.97 (s, 12C, CH_2CH_2CO), 57.68 (s, 4C, CONH*C*), 67.54 (s, 4C, CH_2), 80.62 (s, 12C, CCH_3), 112.96 (s, 8C, *C*H-*benz*), 119.30 (s, 4C, *C-pyr*), 135.58 (s, 8C, *C*-C-*benz*), 135.88 (s, 4C, *C*H-*benz*), 156.88 (s, 4C, *C*-O-*benz*), 167.25 (s, 4C, *C*ONH), 172.48 ppm (s, 12C, $COOCCH_3$); MS (MALDI, dctb): *m/z*: 2501 $[M]^+$, 2502 $[M+H]^+$; HRMS (ESI-TOF, ACN-MeOH): *m/z* calcd for $C_{140}H_{194}N_8Na_2O_{32}$: 1272.6792 $[M+2Na]^{2+}$; found: 1272.6822 $[M+2Na]^{2+}$, 856.4538 $[M+3Na]^{3+}$.

5,10,15,20-(4-(2-Ethoxycarbonyl)-4-(2-phenoxyacetamido)heptanedioic acid)-porphyrin (8): 5,10,15,20-(Di-*tert*-butyl-4-(3-(*tert*-butoxy)-3-oxopropyl)-4-(2-phenoxy-acetamido)heptanedionato)-porphyrin (140 mg; 0.056 mmol) was dissolved in formic adic (40 mL) and stirred for 4 h at room temperature. The formic acid was removed on a rotary evaporator. Subsequently, the product was transferred to toluene and evaporated twice to remove any residual formic acid. The product was finally dried under reduced pressure. Yield: (0.056 mmol), 100%.

^{1}H NMR (400 MHz, 25 °C, DMSO): $\delta = -2.92$ (bs, 2H, N*H*), 1.99 (t, $^3J = 8.0$ Hz, 24H, CH_2CH_2CO), 2.25 (t, $^3J = 8.0$ Hz, 24H, CH_2CH_2CO), 4.77 (s, 8H, CH_2), 7.38 (d, $^3J = 8.4$ Hz, 8H, C*H-benz*), 7.58 (s, 4H, 6), 8.12 (d, $^3J = 8.4$ Hz, 8H, C*H-benz*), 8.87 (s, 8H, C*H-pyrr*), 12.15 ppm (bs, 12H, COO*H*); ^{13}C NMR (400 MHz, 25 °C, DMSO): $\delta = 28.10$ (s, 12C, CH_2CH_2CO), 29.24 (s, 12C, CH_2CH_2CO), 56.96 (s, 4C, CONH*C*), 67.03 (s, 4C, CH_2), 113.14 (s, 8C, *CH-benz*), 119.57 (s, 7C, C-*por*), 131.47 (m, 8C, *CH-pyrr*), 133.99 (s, 4C, *C*-C-*benz*), 135.33 (s, 8C, *CH-benz*), 157.79 (s, 4C, *C*-O-*benz*), 167.23 (s, 4C, *C*ONH), 174.47 ppm (s, 12C, *C*OOH); HRMS (ESI-TOF, ACN-MeOH-HCOOH): *m/z* calcd for $C_{92}H_{98}N_8O_{32}$: 936.3036 $[M+2Na]^{2+}$, 1826.6282 $[M]^+$, 1827.6360 $[M+H]^+$, 1849.6179 $[M+Na]^+$; found: 936.3019 $[M+2Na]^{2+}$, 1827.6279 $[M]^+$, 1827.6279 $[M+H]^+$, 1849.6154 $[M+Na]^+$.

Functionalization of TiO_2 nanoparticles with N1,N7-bis(3-(4-*tert*-butylpyridium-methyl)phenyl)-4-(3-(3-(4-*tert*-butylpyridinium-methyl)phenylamino)-3-oxopropyl)-4-(3,4-dihydroxybenzamido)heptanediamide tribromide (1)

An ethanolic suspension (16.67 mg mL^{-1}) of P-25 TiO_2 nanoparticles (purchased from Evonic) was prepared. For investigation of the functionalization of the TiO_2 surface, a suspension of TiO_2 nanoparticles (washed once with EtOH) was mixed with different quantities of **1** in ethanol [16.272×10^{-7} (**T1**), 4.068×10^{-7} (**T2**), 2.034×10^{-7} (**T3**), 1.017×10^{-7} (**T4**), 0.508×10^{-7} (**T5**), 0.254×10^{-7} (**T6**), and 0 mol mg^{-1} (**T7**)]. The overall TiO_2 concentration for the functionalization was adjusted to 2.08 mg mL^{-1}. The mixture was sonicated for 50 min at room temperature. Subsequently, the suspensions of TiO_2 nanoparticles were centrifuged until the TiO_2 nanoparticles settled completely. The supernatant was removed and the particles were washed three times by the addition of 5 mL ethanol followed by sonication until redispersion was completed, followed by centrifugation until the TiO_2 nanoparticles settled completely. After the last washing step, the TiO_2 nanoparticles were dispersed in ethanol to obtain a particles suspension of 4.81 mg mL^{-1}.

Preparation of tris(hydroxymethyl) aminomethane buffer solutions

A 0.1 M aqueous solution of tris(hydroxymethyl) aminomethane was prepared and subsequently adjusted to pH 9 with 0.1 M HCl solution.

Preparation of poly-(diallyl-dimethylammonium) (PDDA) and poly-(sodium-4-styrene-sulfonato) (PSS) solutions

0.5% PDDA and PSS solutions at pH 3 and pH 4, respectively, were prepared from a 20 wt% solutions in water ($M_w = 400\,000$–$500\,000$; PDDA) and an 18 wt% solution in water ($M_w = 1\,000\,000$; PSS), purchased from Aldrich.

Formation of layer-by-layer assemblies

For the buildup of layer-by-layer assemblies on different substrates, the following sequences were used: 1) dipping of the substrate into a solution of 0.5% $PDDA^+$ at pH 3 for 10 min; 2) rinsing with ethanol/water 1:1 (v/v); 3) dipping into a solution of 0.5% PSS^- at pH 4 for 10 min; 4) rinsing with ethanol/water 1:1 (v/v); 5) dipping into a 10^{-3} M ethanolic suspension of TiO_2 nanoparticles for 10 min; 6) rinsing with ethanol; 7) dipping into a 10^{-3} M TRIS buffer solution at pH 9 of **2** or **3**, respectively, for 10 min; 8) rinsing with ethanol/water 1:1 (v/v). Sequences 1–4) were repeated up to four times. Depending on whether the first deposited layer should con-

sist of porphyrins or TiO_2 nanoparticles, the final polymer layer is $PDDA^+$ or PSS^-, respectively.

Device fabrication

ITO substrates (purchased from Naranjo substrates) were cleaned with water and soap and isopropanol solutions for 15 min in an ultrasonication bath. Immediately, the $PDDA^+$, and PSS^- layers as well as the functionalized TiO_2 nanoparticles and porphyrins were deposited as explained. To complete the devices, we utilized polysulfide electrolytes (i.e., equimolar 3 M Na_2S/S/NaOH) and Cu_2S-based counter electrodes.

Acknowledgements

We gratefully acknowledge funding from the German Research Council (DFG), which, within the framework of its "Excellence Initiative", supports the Cluster of Excellence "Engineering of Advanced Materials" at the University of Erlangen-Nürnberg.

Keywords: catechol · layer-by-layer assemblies · nanoparticles · solar energy conversion · surface chemistry · surface functionalization

[1] a) I. Ahmed, R. Farha, M. Goldmann, L. Ruhlmann, *Chem. Commun.* **2013**, *49*, 496 – 498; b) S. Choi, H. Jin, J. Bang, S. Kim, *J. Phys. Chem. Lett.* **2012**, *3*, 3442 – 3447; c) G. Zhang, K. Pan, W. Zhou, Y. Qu, Q. Pan, B. Jiang, G. Tian, G. Wang, Y. Xie, Y. Dong, X. Miao, C. Tian, *Dalton Trans.* **2012**, *41*, 12683 – 12689.

[2] a) E. M. Shchukina, D. G. Shchukin, *Adv. Drug Delivery Rev.* **2011**, *63*, 837 – 846; b) K. Sato, J.-i. Anzai, *Molecules* **2013**, *18*, 8440 – 8460.

[3] D. M. DeLongchamp, P. T. Hammond, *Adv. Funct. Mater.* **2004**, *14*, 224 – 232.

[4] T. R. Farhat, P. T. Hammond, *Adv. Funct. Mater.* **2005**, *15*, 945 – 954.

[5] N. Dal'Acqua, F. R. Scheffer, R. Boniatti, B. V. M. da Silva, J. V. de Melo, J. da Silva Crespo, M. Giovanela, M. B. Pereira, D. E. Weibel, G. Machado, *J. Phys. Chem. C* **2013**, *117*, 23235 – 23243.

[6] a) G. Decher, J.-D. Hong, *Makromol. Chem. Macromol. Symp.* **1991**, *46*, 321 – 327; b) G. Decher, *Science* **1997**, *277*, 1232 – 1237.

[7] H. Zhang, J. Rühe, *Macromolecules* **2003**, *36*, 6593 – 6598.

[8] a) N. G. Hoogeveen, M. A. Cohen Stuart, G. J. Fleer, *Langmuir* **1996**, *12*, 3675 – 3681; b) M.-A. Neouze, *J. Mater. Sci.* **2013**, *48*, 7321 – 7349; c) G. Wu, X. Zhang, *Polymer Thin Films, Abbass A Hashim (Ed.)* **2010**.

[9] a) Y. M. Lvov, G. Decher, H. Möhwald, *Langmuir* **1993**, *9*, 481 – 486; b) C. C. Buron, C. Filiâtre, *J. Colloid Interface Sci.* **2014**, *413*, 147 – 153; c) Y. Tan, U. H. Yildiz, W. Wei, J. H. Waite, A. Miserez, *Biomacromolecules* **2013**, *14*, 1715 – 1726; d) S. Fujita, S. Shiratori, *Nanotechnology* **2005**, *16*, 1821 – 1827; e) V. V. Tsukruk, F. Rinderspacher, V. N. Bliznyuk, *Langmuir* **1997**, *13*, 2171 – 2176.

[10] K. Rosenlehner, T. Schunk, N. Jux, M. Brettreich, A. Hirsch, *Org. Biomol. Chem.* **2008**, *6*, 2697 – 2705.

[11] a) E. R. Kleinfeld, G. S. Ferguson, *Science* **1994**, *265*, 370 – 373; b) Y. M. Lvov, H. Haas, G. Decher, H. Möhwald, *Langmuir* **1994**, *10*, 4232 – 4236; c) V. V. Tsukruk, *Adv. Mater.* **1998**, *10*, 253 – 257; d) J. H. Fendler, *Chem. Mater.* **1996**, *8*, 1616 – 1624; e) S. Srivastava, N. A. Kotov, *Acc. Chem. Res.* **2008**, *41*, 1831 – 1841; f) M. Shao, J. Han, W. Shi, M. Wei, X. Duan, *Electrochem. Commun.* **2010**, *12*, 1077 – 1080; g) A. R. G. Smith, J. L. Ruggles, A. Yu, I. R. Gentle, *Langmuir* **2009**, *25*, 9873 – 9878.

[12] B. P. Pichon, P. Louet, O. Felix, M. Drillon, S. Begin-Colin, G. Decher, *Chem. Mater.* **2011**, *23*, 3668 – 3675.

[13] N. A. Kotov, I. Dékány, J. H. Fendler, *J. Phys. Chem.* **1995**, *99*, 13065 – 13069.

[14] J. Schmitt, G. Decher, W. J. Dressick, S. L. Brandow, R. E. Geer, R. Shashidhar, J. M. Calvert, *Adv. Mater.* **1997**, *9*, 61 – 65.

[15] a) W.-H. Khoh, J.-D. Hong, *Colloids Surf. A* **2013**, *436*, 104 – 112; b) B. H. R. Suryanto, X. Lu, C. Zhao, *J. Mater. Chem. A* **2013**, *1*, 12726 – 12731.

[16] X. Chen, S. S. Mao, *Chem. Rev.* **2007**, *107*, 2891 – 2959.

[17] a) D. Chen, R. A. Caruso, *Adv. Funct. Mater.* **2013**, *23*, 1356 – 1374; b) M. Grätzel, *J. Photochem. Photobiol. A* **2004**, *164*, 3 – 14; c) M. M. Byranvand, A. N. Kharat, M. H. Bazargan, *Nano-Micro Lett.* **2012**, *4*, 253 – 266; d) Y. Horiuchi, T. Toyao, M. Takeuchi, M. Matsuoka, M. Anpo, *Phys. Chem. Chem. Phys.* **2013**, *15*, 13243 – 13253.

[18] W. M. Campbell, K. W. Jolley, P. Wagner, K. Wagner, P. J. Walsh, K. C. Gordon, L. Schmidt-Mende, M. K. Nazeeruddin, Q. Wang, M. Gratzel, D. L. Officer, *J. Phys. Chem. C* **2007**, *111*, 11760 – 11762.

[19] a) H. Tokuhisa, P. T. Hammond, *Adv. Funct. Mater.* **2003**, *13*, 831 – 839; b) T. Hasobe, S. Hattori, P. V. Kamat, S. Fukuzumi, *Tetrahedron* **2006**, *62*, 1937 – 1946; c) T. Hasobe, S. Hattori, P. V. Kamat, Y. Urano, N. Umezawa, T. Nagano, S. Fukuzumi, *Chem. Phys.* **2005**, *319*, 243 – 252; d) C. Yang, Z. Yang, H. Gu, C. K. Chang, P. Gao, B. Xu, *Chem. Mater.* **2008**, *20*, 7514 – 7520; e) M. Funes, P. Zabel, T. Dittrich, E. N. Durantini, L. Otero, *Phys. Status solidi C* **2010**, *7*, 280 – 283; f) J. E. Kroeze, T. J. Savenije, J. M. Warman, *J. Photochem. Photobiol. A* **2002**, *148*, 49 – 55; g) C.-F. Lo, L. Luo, E. W.-G. Diau, I.-J. Chang, C.-Y. Lin, *Chem. Commun.* **2006**, 1430.

[20] a) J. Cao, D.-C. Hu, J.-C. Liu, R.-Z. Li, N.-Z. Jin, *Org. Electron.* **2014**, *15*, 509 – 516; b) M. T. Brumbach, A. K. Boal, D. R. Wheeler, *Langmuir* **2009**, *25*, 10685 – 10690; c) J. Cao, D.-C. Hu, J.-C. Liu, R.-Z. Li, N.-Z. Jin, *Inorg. Chim. Acta* **2014**, *414*, 165 – 169; d) Y. Wu, J.-C. Liu, J. Cao, R.-Z. Li, N.-Z. Jin, *Res. Chem. Intermediates* **2014**, 1 – 10; e) H. B. Gobeze, S. K. Das, F. D'Souza, *J. Phys. Chem. C* **2014**, *118*, 16660 – 16671; f) L. A. Martini, G. F. Moore, R. L. Milot, L. Z. Cai, S. W. Sheehan, C. A. Schmuttenmaer, G. W. Brudvig, R. H. Crabtree, *J. Phys. Chem. C* **2013**, *117*, 14526 – 14533; g) C. F. A. Negre, R. L. Milot, L. A. Martini, W. Ding, R. H. Crabtree, C. A. Schmuttenmaer, V. S. Batista, *J. Phys. Chem. C* **2013**, *117*, 24462 – 24470.

[21] J. H. Yang, Y. M. Chen, Y. B. Bai, M. Xian, D. F. Shen, Y. Q. Wang, S. R. Du, R. Lu, T. J. Li, Y. Wu, W. Q. Xu, *Supramol. Sci.* **1998**, *5*, 599 – 602.

[22] M. C. So, S. Jin, H.-J. Son, G. P. Wiederrecht, O. K. Farha, J. T. Hupp, *J. Am. Chem. Soc.* **2013**, *135*, 15698 – 15701.

[23] a) F. Hasani Bijarbooneh, Y. Zhao, J. H. Kim, Z. Sun, V. Malgras, S. H. Aboutalebi, Y.-U. Heo, M. Ikegami, S. X. Dou, G. Franks, *J. Am. Ceram. Soc.* **2013**, *96*, 2636 – 2643; b) R. A. French, A. R. Jacobson, B. Kim, S. L. Isley, R. L. Penn, P. C. Baveye, *Environ. Sci. Technol.* **2009**, *43*, 1354 – 1359.

[24] M.-A. Neouze, U. Schubert, *Monatsh. Chem.* **2008**, *139*, 183 – 195.

[25] a) N. Erathodiyil, J. Y. Ying, *Acc. Chem. Res.* **2011**, *44*, 925 – 935; b) F. Iskandar, *Adv. Powder Technol.* **2009**, *20*, 283 – 292; c) S. T. Kim, K. Saha, C. Kim, V. M. Rotello, *Acc. Chem. Res.* **2013**, *46*, 681 – 691; d) R. Mout, D. F. Moyano, S. Rana, V. M. Rotello, *Chem. Soc. Rev.* **2012**, *41*, 2539 – 2543; e) T. Banerjee, S. Kaniyankandy, A. Das, H. N. Ghosh, *J. Phys. Chem. C* **2013**, *117*, 3084 – 3092.

[26] a) A. Vaccaro, J. Hierrezuelo, M. Skarba, P. Galletto, J. r. Kleimann, M. Borkovec, *Langmuir* **2009**, *25*, 4864 – 4867; b) E. Rampazzo, E. Brasola, S. Marcuz, F. Mancin, P. Tecilla, U. Tonellato, *J. Mater. Chem.* **2005**, *15*, 2687 – 2695; c) Y. Kim, S. An, S. Kim, J. H. Park, H. A. Son, H. T. Kim, K.-D. Suh, J. W. Kim, *Polymer* **2013**, *54*, 5609 – 5614; d) H. Jin, J. Nam, J. Park, S. Jung, K. Im, J. Hur, J.-J. Park, J.-M. Kim, S. Kim, *Chem. Commun.* **2011**, *47*, 1758 – 1760.

[27] a) H. Lee, S. M. Dellatore, W. M. Miller, P. B. Messersmith, *Science* **2007**, *318*, 426 – 430; b) H. Lee, N. F. Scherer, P. B. Messersmith, *Proc. Natl. Acad. Sci. USA* **2006**, *103*, 12999 – 13003; c) B. Malisova, S. Tosatti, M. Textor, K. Gademann, S. Zürcher, *Langmuir* **2010**, *26*, 4018 – 4026; d) Q. Ye, F. Zhou, W. Liu, *Chem. Soc. Rev.* **2011**, *40*, 4244 – 4258; e) H. Gulley-Stahl, P. A. Hogan, W. L. Schmidt, S. J. Wall, A. Buhrlage, H. A. Bullen, *Environ. Sci. Technol.* **2010**, *44*, 4116 – 4121; f) J. Saiz-Poseu, J. Sedó, B. García, C. Benaiges, T. Parella, R. Alibés, J. Hernando, F. Busqué, D. Ruiz-Molina, *Adv. Mater.* **2013**, *25*, 2066 – 2070; g) J. Sedó, J. Saiz-Poseu, F. Busqué, D. Ruiz-Molina, *Adv. Mater.* **2013**, *25*, 653 – 701; h) C. Creutz, M. H. Chou, *Inorg. Chem.* **2008**, *47*, 3509 – 3514; i) I. A. Janković, Z. V. Šaponjić, M. I. Čomor, J. M. Nedeljković, *J. Phys. Chem. C* **2009**, *113*, 12645 – 12652; j) D. S. Hwang, M. J. Harrington, Q. Lu, A. Masic, H. Zeng, J. H. Waite, *J. Mater. Chem.* **2012**, *22*, 15530 – 15533.

[28] J.-F. Gnichwitz, R. Marczak, F. Werner, N. Lang, N. Jux, D. M. Guldi, W. Peukert, A. Hirsch, *J. Am. Chem. Soc.* **2010**, *132*, 17910 – 17920.

[29] A. McKillop, J.-C. Fiaud, R. P. Hug, *Tetrahedron* **1974**, *30*, 1379 – 1382.

[30] a) J. S. Lindsey, I. C. Schreiman, H. C. Hsu, P. C. Kearney, A. M. Margueregtaz, *J. Org. Chem.* **1987**, *52*, 827 – 836; b) J. S. Lindsey, R. W. Wagner, *J. Org. Chem.* **1989**, *54*, 828 – 836; c) J. S. Lindsey, K. A. MacCrum, J. S. Tyhonas, Y.-Y. Chuang, *J. Org. Chem.* **1994**, *59*, 579 – 587.

[31] a) B. Neises, W. Steglich, *Angew. Chem.* **1972**, *105*, 1368 – 1376; b) B. Neises, W. Steglich, *Angew. Chem.* **1978**, *90*, 556 – 557.
[32] a) G. R. Newkome, R. K. Behera, C. N. Moorefield, G. R. Baker, *J. Org. Chem.* **1991**, *56*, 7162 – 7167; b) G. R. Newkome, A. Nayak, R. K. Behera, C. N. Moorefield, G. R. Baker, *J. Org. Chem.* **1992**, *57*, 358 – 362; c) M. Brettreich, A. Hirsch, *Synlett* **1988**, 1396 – 1398.
[33] J. Moser, S. Punchihewa, P. P. Infelta, M. Grätzel, *Langmuir* **1991**, *7*, 3012 – 3018.
[34] a) T. Imae, K. Muto, S. Ikeda, *Colloid Polym. Sci.* **1991**, *269*, 43 – 48; b) D. L. Liao, G. S. Wu, B. Q. Liao, *Colloids Surf. A* **2009**, *348*, 270 – 275.
[35] V. V. Tsukruk, V. N. Bliznyuk, D. Visser, A. L. Campbell, T. J. Bunning, W. W. Adams, *Macromolecules* **1997**, *30*, 6615 – 6625.
[36] D. M. Guldi, F. Pellarini, M. Prato, C. Granito, L. Troisi, *Nano Lett.* **2002**, *2*, 965 – 968.

Received: August 29, 2014
Published online on ■■ ■■, 0000

FULL PAPER

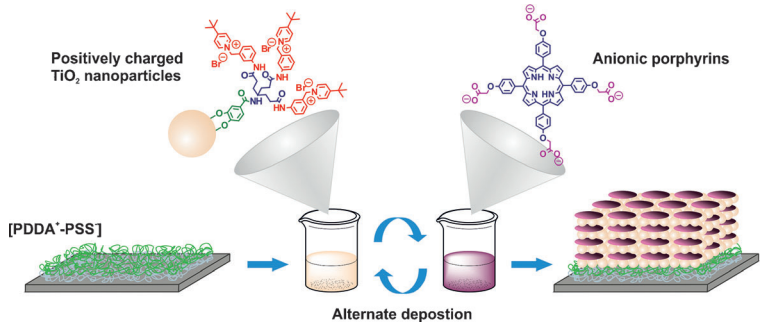

Multilayer assemblies: Layer-by-layer assemblies of positively charged TiO_2 nanoparticles (NPs) and anionic porphyrins are applied in solar-energy conversion schemes. TiO_2 NPs are functionalized with permanent positively charged catechol molecules, leading to stable ethanolic NP suspensions. Alternate deposition of these NPs and anionic porphyrins through simple dip coating results in multilayer assemblies formed through electrostatic attraction (see figure).

Solar Energy Conversion

*A. Burger, R. D. Costa, V. Lobaz, W. Peukert, D. M. Guldi, A. Hirsch**

■■ – ■■

Layer-by-Layer Assemblies of Catechol-Functionalized TiO_2 Nanoparticles and Porphyrins through Electrostatic Interactions